

# A Large-Diameter Hollow-Shaft Cryogenic Motor Based on a Superconducting Magnetic Bearing for Millimeter-Wave Polarimetry

B. R. Johnson,<sup>1, a)</sup> F. Columbro,<sup>2</sup> D. Araujo,<sup>1</sup> M. Limon,<sup>1</sup> B. Smiley,<sup>1</sup> G. Jones,<sup>1</sup> B. Reichborn-Kjennerud,<sup>1</sup> A. Miller,<sup>3</sup> and S. Gupta<sup>1</sup>

<sup>1)</sup>*Department of Physics, Columbia University, New York, NY 10027, USA*

<sup>2)</sup>*Dipartimento di Fisica, Università di Roma La Sapienza, 00185 Roma, Italy*

<sup>3)</sup>*Department of Physics and Astronomy, University of Southern California, Los Angeles, CA 90089, USA*

(Dated: 6 October 2017)

In this paper we present the design and measured performance of a novel cryogenic motor based on a superconducting magnetic bearing (SMB). The motor is tailored for use in millimeter-wave half-wave plate (HWP) polarimeters, where a HWP is rapidly rotated in front of a polarization analyzer or polarization-sensitive detector. This polarimetry technique is commonly used in cosmic microwave background (CMB) polarization studies. The SMB we use is composed of fourteen yttrium barium copper oxide (YBCO) disks and a contiguous neodymium iron boron (NdFeB) ring magnet. The motor is a hollow-shaft motor because the HWP is ultimately installed in the rotor. The motor presented here has a 100 mm diameter rotor aperture. However, the design can be scaled up to rotor aperture diameters of approximately 500 mm. Our motor system is composed of four primary subsystems: (i) the rotor assembly, which includes the NdFeB ring magnet, (ii) the stator assembly, which includes the YBCO disks, (iii) an incremental encoder, and (iv) the drive electronics. While the YBCO is cooling through its superconducting transition, the rotor is held above the stator by a novel hold and release mechanism (HRM). The encoder subsystem consists of a custom-built encoder disk read out by two fiber optic readout sensors. For the demonstration described in this paper, we ran the motor at 50 K and tested rotation frequencies up to approximately 10 Hz. The feedback system was able to stabilize the the rotation speed to approximately 0.4%, and the measured rotor orientation angle uncertainty is less than 0.15 deg. Lower temperature operation will require additional development activities, which we will discuss.

## I. INTRODUCTION

Half-wave plate (HWP) polarimetry is a technique that is now commonly used for cosmic microwave background (CMB) polarization studies<sup>1–7</sup>. With this technique a HWP is rotated in the telescope beam in front of a polarization analyzer. The linearly polarized component of the incoming radiation is rotated by the HWP, ultimately producing a modulated signal in the emerging detector data stream at four times the rotation frequency of the HWP<sup>8</sup>. If the HWP is rapidly rotated, then this approach allows the observer to move the polarization signals away from problematic noise features in the detector bandwidth, such as low-frequency  $1/f$  noise, thereby maximizing the sensitivity of the instrument and possibly enabling observations on larger angular scales<sup>9</sup>. The approach can also be used to help mitigate the effect of some kinds of instrument-induced systematic errors<sup>10</sup>, but for this paper we are primarily interested in the technical aspects of rapid HWP rotation and ways to produce high-frequency signal modulation.

For CMB polarization studies there are three primary performance requirements to consider for the HWP rotation system. First, thermal emission from the optical elements in the polarimeter – such as the HWP – must be minimized to maximize instrument sensitivity because the noise from state-of-the-art millimeter-wave

detector systems is commonly limited by the random arrival of photons. Since the CMB is a 2.7 K blackbody, the brightness temperature of any thermal emission in the instrument ideally should be suppressed to approximately this level or below. Second, because the detector systems are photon-noise limited, large arrays of independent detectors are required to average down the instrument noise. This requirement has created the need for large-throughput ( $A\Omega$  product) telescopes, which ultimately means the rotating HWP must have a large diameter (between approximately 200 mm and 500 mm). Third, to accurately reconstruct the polarization patterns on the sky, the HWP orientation must be measured to approximately 0.2 deg or better<sup>10</sup>. These three requirements together create the need for a speed-variable, large-diameter, hollow-shaft rotator that operates at cryogenic temperatures. The orientation of the rotator must be precisely measured, and the cryogenic parts of the system cannot generate appreciable amounts of heat from mechanisms like stick-slip friction.

To solve this problem, the balloon-borne EBEX experiment developed,<sup>11–14</sup> built, and deployed<sup>15</sup> a HWP rotator based on a superconducting magnetic bearing (SMB). In the EBEX SMB, a permanent neodymium iron boron (NdFeB) ring magnet assembly was levitated above a matching ring of yttrium barium copper oxide (YBCO) via field cooling. SMBs based on high-temperature superconductors are attractive for this application because flux pinning allows any-orientation operation after the bearing rotor is levitating<sup>16</sup>. The EBEX HWP, which

<sup>a)</sup>bradley.johnson@columbia.edu

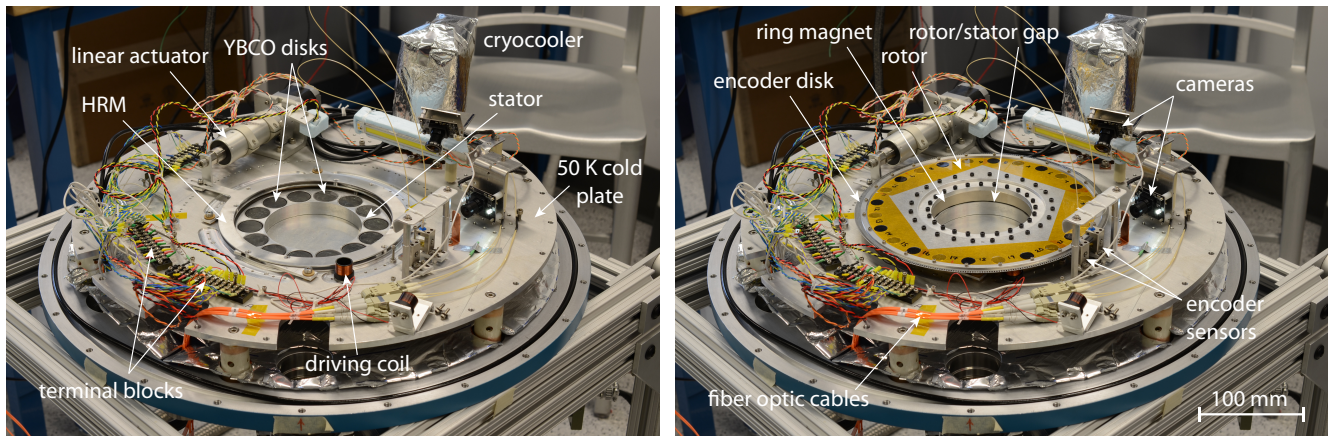


FIG. 1. Photographs of the motor system installed on the 50 K cold plate of the cryostat. In the photograph on the left, the rotor is removed exposing the YBCO disks and the hold-and-release mechanism (HRM). In the photograph on the right, the HRM is engaged, holding the rotor in place above the stator. The 2 mm gap between the rotor and the stator is visible. The rotor and HRM are shown in more detail in Figure 2. Excluding the linear actuator, the overall height of the motor is 38 mm, and the fully assembled rotor and stator fit inside a circular footprint approximately 280 mm in diameter. The vacuum shell of the cryostat and the 50 K radiation shield were removed for these photographs, so the motor elements are visible.

was mounted inside the rotor of the SMB, was ultimately rotated by a motor mounted outside the cryostat. The driveshaft of this motor passed through the cryostat shell using a rotary vacuum feedthrough and turned a small-diameter pulley wheel inside the cryostat that was coupled to the rotor of the SMB via a Kevlar belt.

Many groups around the world are developing rotators for HWP polarimetry using different approaches<sup>4, 5</sup>. In this paper we present the design and measured performance of one novel approach: a hollow-shaft, cryogenic motor based on an SMB. We describe the motor hardware in Section II, and the characterization measurement results in Section III. The success of this proof-of-concept prototype motor justifies future development activities, which are discussed in Section IV.

## II. METHODS

Our motor system is composed of four primary subsystems: (i) the rotor assembly, (ii) the stator assembly, which includes the YBCO, (iii) the encoder, and (iv) the drive electronics. An overview photograph of the motor system is shown in Figure 1, and the key elements in each subsystem are described in Sections II A to II E.

Our design builds from the EBEX design and makes three critical advancements. First, our hold-and-release mechanism (HRM), which is described in Section II C, could prove to be more mechanically robust than the EBEX design that used spring loaded “grippers” positioned by a linear actuator and a Kevlar-string pulley system. We show in this paper that our HRM functions cryogenically as designed, and although our prototype hollow-shaft diameter is just 100 mm, our HRM design is scalable and can ultimately accommodate HWP diameters between 100 mm and 500 mm or more<sup>17,18</sup>. Second, the rotor can be driven with a single electromagnet coil pair, so the Kevlar belt is not needed in our approach.

This design change removes a thermal load on the rotor, which should help minimize the HWP temperature. Third, our optical encoder design, which is based on optical fibers (Section II D), moves the required light sources and photodetectors outside the cryostat, which removes a heat load on the cryogenics, and our quadrature readout approach provides additional rotation direction information.

Since this motor is the product of a proof-of-concept study, two additional choices constrained our design. First, for convenience at this early development stage, we targeted 50 K operation, noting that lower-temperature operation may be more desirable in the future. Second, after considering segmented magnets and magnet tiles for the ring on the rotor, we decided that a contiguous magnet was the most promising in terms of SMB performance. Therefore, the scale of our prototype motor was set by the largest commercially available off-the-shelf NdFeB ring magnet we could find. We then tailored the HRM to the size of this magnet. Larger magnets can be fabricated as custom parts, so our approach is scalable.

### A. Cryostat

The motor is mounted inside a custom-built aluminum cryostat<sup>19</sup> on an aluminum cold plate 530 mm in diameter and 6.4 mm thick. The cold plate is cooled to 50 K by a two-stage Gifford-McMahon (GM) cryocooler<sup>20</sup>. For this work, only the 50 K stage of the GM cooler is used; the second, 20 K stage is unloaded, which gives the 50 K stage more cooling power. A cylindrical radiation shield mounted to the cold plate surrounds the motor to reject 300 K radiation from the vacuum shell of the cryostat. The radiation shield is 530 mm in diameter and 350 mm tall. The temperature of the system is monitored with four-wire platinum resistor temperature sensors<sup>21</sup>. One sensor is mounted directly on the cold head of the

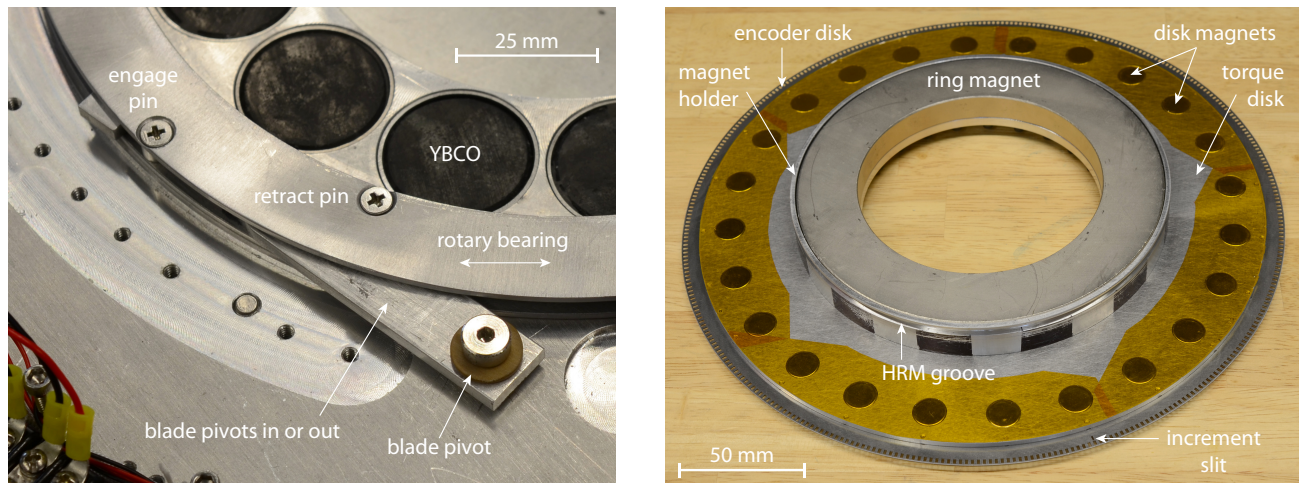


FIG. 2. **Left:** A photograph of one of the three hold-and-release mechanism blades. The linear actuator shown in Figure 1 is used to move the rotary bearing. If the rotary bearing moves clockwise (in the photograph), then the retract pin pivots the blade away from the rotor. If the rotary bearing moves counterclockwise, then the engage pin pivots the blade toward the rotor and ultimately into its HRM groove. **Right:** A photograph of the reverse side of the rotor (relative to the view shown in Figure 1). The rotor builds from an aluminum ring-magnet holder that has the HRM groove. A separate aluminum “torque disk” serves as a mount for the disk magnets used in the drive system and a mount for the encoder ring. The ring-magnet holder and the torque disk are assembled with steel screws, and the ring magnet is held in place using the attractive force between the ring magnet and these steel screws; no epoxy was used. The steel screws (black) are visible in Figure 1. After the YBCO in the stator cools below its superconducting transition temperature, the linear actuator is retracted, opening the HRM, releasing the rotor and allowing it to levitate freely.

GM cryocooler, while the other three are mounted on the cold plate near the YBCO disks on the stator. The thermometers are read out using commercially available electronics<sup>22</sup>.

The vacuum shell on the cryostat contains four KF50 ports. The first port is used for vacuum pumping<sup>23</sup>. The second port hosts a USB 2.0 vacuum feedthrough<sup>24</sup> that is used to provide power and signal I/O wiring for two USB cameras (see Section III A). The third port hosts a custom-built vacuum feedthrough for the optical fibers used in the encoder system<sup>25</sup>. The fourth port hosts a vacuum feedthrough for a 41-pin connector<sup>26</sup>, which is used for all additional wiring. The electrical current driving the motor is appreciable so we use 24 AWG copper wire for the two drive-coil wires (see Section II E). Otherwise, to minimize the thermal loading on the 50 K stage we use 32 AWG manganin 290 wire<sup>27</sup>. Terminal blocks mounted on the cold plate (see Figure 1) serve as a thermal intercept for the wiring and a convenient electrical interconnect.

## B. Superconducting Magnetic Bearing

The stator of the superconducting magnetic bearing consists of fourteen YBCO disks<sup>28</sup> that are arranged in a ring. This ring can be easily seen in the left panel of Figure 1. Each YBCO disk is 13 mm tall, 25 mm in diameter and is specified to generate 60 N of levitation force at 77 K assuming the magnet/YBCO separation distance is 9 mm and the permanent magnet has a 0.5 T field at its surface. YBCO is a brittle material, so before assembly,

each disk was first mounted in a thin-walled cylindrical aluminum cup with epoxy<sup>29</sup>. Each cup is open on the top and has tapped mounting holes on the bottom. Each disk/cup assembly was then screwed into a recess in a custom-built aluminum holder on the stator. The holder defined the ring shape. This mounting approach yields good thermal contact between the YBCO and the 50 K cold plate, while at the same time, it allows disassembly and disk replacement.

The rotor of the SMB is an N42 grade NdFeB ring magnet<sup>30</sup> with a nominal pull force of 930 N and a residual flux density of 1.3 T. The ring magnet is 13 mm thick, it has a 150 mm outer diameter, a 100 mm inner diameter, and a mass of 0.88 kg. To provide durability and protection against corrosion, the magnet was coated with a nickel-copper-nickel trilayer. During cryogenic operation, the rotor levitated above the stator with a rotor/stator separation distance of approximately 2 mm.

## C. Hold and Release Mechanism

While the YBCO cools, the rotor is held above the stator by the hold and release mechanism shown in Figure 2. The HRM design was inspired by an iris diaphragm. It is composed of (i) a large-diameter, custom-built rotary bearing that encircles the YBCO ring on the stator, (ii) three pivoting blades, (iii) engage and retract pins on the rotary bearing that pivot the blades in and out, and (iv) a linear actuator<sup>31</sup> that moves the rotary bearing by pushing or pulling tangentially on its edge. During operation, as the linear actuator moves, the rotary bearing turns,

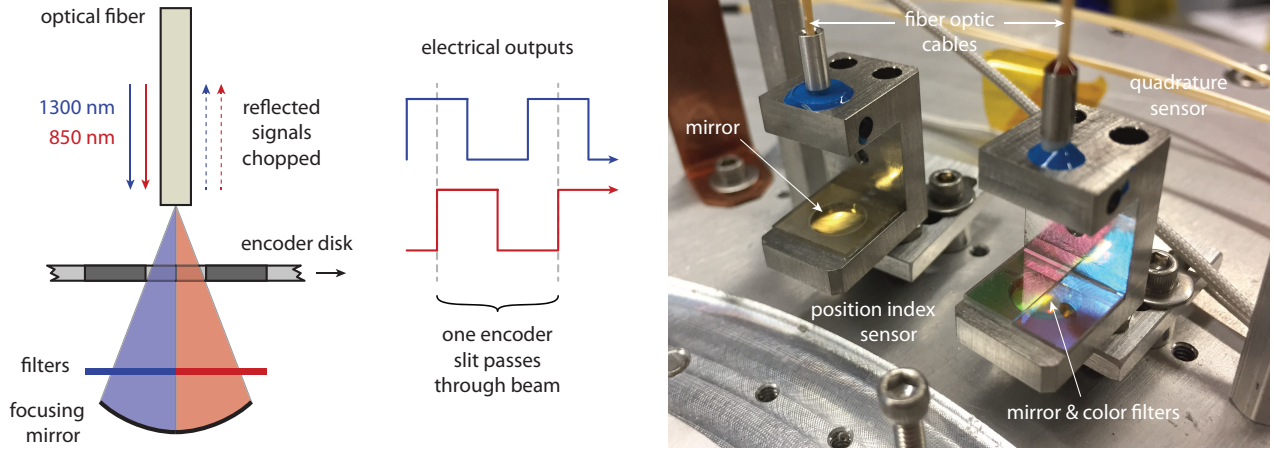


FIG. 3. **Left:** Schematic illustrating how the quadrature encoder sensor works. Two wavelengths of light are carried into the cryostat on a single optical fiber. The light emitted from the end of the optical fiber is filtered and then refocused back into the fiber with a mirror. The filters are arranged so the left half of the reflected beam passes 1300 nm, while the right half passes 850 nm. As the incremental encoder disk passes by the beam is chopped on and off. However, because one filter precedes the other, the two wavelengths are chopped out of phase, and this quarter-wave phase offset indicates the rotation direction. The encoder readout transforms the optical signals into a quadrature electrical outputs, which can be used in the feedback loop and to determine the orientation angle of the rotor. **Right:** A photograph of the two encoder sensors mounted in the cryostat on the 50 K cold plate. For clarity, the encoder disk is not shown. Note that the position index sensor detects a single increment slit on a separate track of the encoder disk each rotation (see the right panel of Figure 2). Therefore, only a single wavelength of light (850 nm) is used for this sensor.

and the blades move in or out. When the motor is at room temperature the linear actuator is extended, and the HRM blades slot into a groove on the edge of the rotor, thereby holding the rotor fixed above the stator both vertically and laterally. After the YBCO is cooled below the superconducting transition temperature (93 K) the linear actuator is retracted, causing the HRM to remove the blades, release the rotor, and allow the rotor to levitate freely above the stator. The linear actuator, which was designed to function at cryogenic temperatures, is powered by a two-phase, high-torque, hybrid stepper motor<sup>32</sup> with a resolution of 95 steps per millimeter and 200 steps per revolution. The motor driver<sup>33</sup> was pre-programmed to either extend or retract the actuator by 25 mm upon activation. Limit switches provided with the stepper motor prevent the linear actuator from overextending and damaging the HRM or the rotor.

#### D. Encoder

The encoder system consists of a custom-built incremental encoder disk read out by two optical readout sensors<sup>34</sup>. The right panel of Figure 2 shows a photograph of the encoder disk, and Figure 3 illustrates the operation of the encoder readout system.

The encoder disk, which serves as a photo interrupter, has 360 equally spaced slits around its perimeter, and it is mounted to the edge of the “torque disk” on the rotor (see Figure 2 and Section II E). The encoder disk was laser cut from 400  $\mu\text{m}$  thick stainless steel sheet metal. Each slit is approximately 2 mm long and 1.11 mm wide at its widest point. The outer diameter of the encoder

disk is 254 mm, while the inner diameter is 229 mm.

Two wavelengths of light (1300 and 850 nm) are generated by sources outside the cryostat<sup>35</sup> and fed into the cryostat on a optical fiber that passes through the aforementioned custom-built, fiber-optic vacuum feedthrough. The total diameter of each optical fiber is 125  $\mu\text{m}$ , and the core diameter is 62.5  $\mu\text{m}$ . Inside the cryostat, the end of the optical fiber is mounted perpendicular to the encoder disk near the slits using custom-built titanium mounts. Light emitted from the end of the optical fiber is filtered and then refocused back into the fiber with a spherical mirror. This reflected light is detected outside the cryostat with photodetectors. The filters, which are mounted in front of the focusing mirror, are arranged so the left half of the reflected beam passes only 1300 nm light, while the right half passes only 850 nm light. During operation, the emerging beam passes through, or is interrupted by, the slits in the encoder disk. However, because one filter precedes the other, the two wavelengths are chopped out of phase, and this quarter-wave phase offset indicates the rotation direction (see left panel of Figure 3). The encoder readout transforms the optical signals into quadrature electrical square wave signals, which are used in the feedback loop to determine the orientation angle, direction, and angular speed of the rotor. Note that inside the optical fiber, light is traveling in both directions. The in-bound light beams are continuous, while the out-bound beams are chopped.

A second optical sensor detects a single index position slit on a separate inner track of the encoder disk using an 850 nm light beam<sup>36</sup>. This index position slit resets an internal counter in the feedback system each revolution, and it is used to ensure that the orientation angle of the rotor is reset to zero after each complete rotation of the

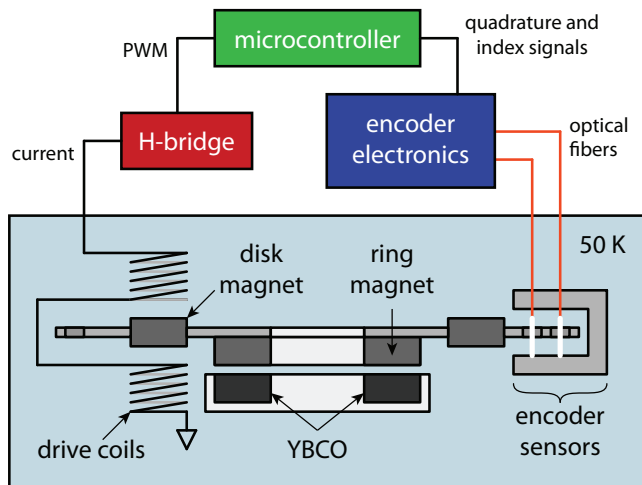


FIG. 4. A schematic showing the feedback loop of the motor control system. The user first inputs the target rotation frequency into the software on the microcontroller. The microcontroller then sends a PWM signal to the H-bridge, which controls the current in the drive coils. The primary motor elements mounted at 50 K are shown in cross section. The magnetic field produced by the coils interacts with the ring of permanent disk magnets that are mounted on the rotor (see Figure 2). As the rotor turns, the optical encoder generates the index position pulse and the quadrature square-wave signals that are shown in Figure 3. These signals are fed back into the microcontroller, which uses them to compute the angular position and speed of the rotor. The output PWM signal is automatically adjusted by the microcontroller if the measured rotation frequency is different from the input target rotation frequency.

encoder disk (see right panel of Figure 2).

### E. Drive System

The drive system for the motor uses a proportional-integral (PI) feedback loop composed of a microprocessor, an H-bridge<sup>37</sup>, two hollow-core electromagnet coils<sup>38</sup>, and an optical encoder. The electromagnet coils are 10.8 mm long, have an inner diameter of 13.4 mm, an outer diameter of 16.0 mm, and are composed of approximately 120 turns of insulated 30 AWG copper wire. A schematic of the feedback loop is shown in Figure 4. We chose to use the Arduino 2 microcontroller because it has a fast 84 MHz clock and pulse width modulation (PWM) output pins. Rotation frequencies between 2.5 and 25 Hz (150 and 1500 RPM) are useful because the  $1/f$  knee of low-frequency noise in millimeter-wave observations is commonly 10 Hz or below<sup>2</sup> and millimeter-wave detector systems can have up to approximately 100 Hz or more of usable bandwidth<sup>39</sup>. For the demonstration described in this paper, we tested rotation frequencies up to approximately 10 Hz.

During operation, the rotation direction and the target rotation frequency of the rotor are defined by the user as input parameters in the software on the microcontroller. The microcontroller then sends a PWM signal to a standard H-bridge circuit that controls both the mag-

nitude and polarity of the current through the coils. The time-varying magnetic field produced by the coils interacts with the ring of 24 permanent disk magnets that are mounted on the torque disk on the rotor (see Figure 2). The disk magnets<sup>40</sup> are 13 mm in diameter, 3.2 mm thick, made from grade N42 nickel-copper-nickel plated NdFeB, and arranged so any two neighboring magnets in the ring have opposite polarity. The drive coils are mounted approximately 2 mm from the disk magnets. The torque disk is used to separate the disk magnets from the ring magnet and the YBCO. This ensures that flux from the disk magnets is not pinned in the YBCO. It also increases the torque applied by the drive coil pair because the force is applied at a larger radius.

When the rotor is initially at rest, strong current pulses are sent to the coils to start the rotor turning. When the position index sensor detects a pulse for the first time the current modulation begins. During normal operation, the optical encoder generates the index position pulse and the quadrature square-wave signals that are shown in Figure 3. These signals are fed back into the microcontroller, which uses them to compute the angular position and speed of the rotor. The angular speed of the rotor is the feedback signal for the PI loop. The rotor speed and orientation measurements are also output and stored on a computer as time-ordered data.

## III. RESULTS

### A. Visual Inspection

Our cryostat does not have a window. Therefore, we installed two USB 2.0 cameras<sup>41</sup> inside the cryostat to watch the motor turn and to observe the HRM during operation (see Figure 5). The cameras we selected use the 1/4 inch OmniVision OV5640 CMOS sensor, which has 1.4  $\mu\text{m}$  square pixels and a resolution of  $2592 \times 1944$ . The camera modules use threaded M12 lens mounts, and can deliver either still photographs or video at up to 30 fps. With camera #1 we use an F/2.0 lens with a 2.6 mm focal length to observe the system as a whole from the top of the motor. Camera #2 uses an F/2.6 lens with a 2.8 mm focal length to monitor any lateral movement in the rotor from the side. The camera power and signal I/O were fed into the cryostat through the aforementioned USB 2.0 vacuum feedthrough (see Section II A).

These cameras are not nominally rated for cryogenic operation. Therefore, we took precautions to make sure they would function properly in our system. We first mounted the bare camera modules on custom aluminum interface plates with standoffs to prevent electrical shorts on the back side of the printed circuit boards. We then mounted these assemblies on ceramic standoffs<sup>42</sup> to reduce the thermal conductance between the cameras and the 50 K cold plate. In the vacuum environment inside the cryostat, there is no convective heat transfer and radiative heat transfer is negligible. Therefore in equilibrium, waste electrical heat flowing into the camera module is equal to the heat flowing out of the camera module through the ceramic standoff. For our thermal design,

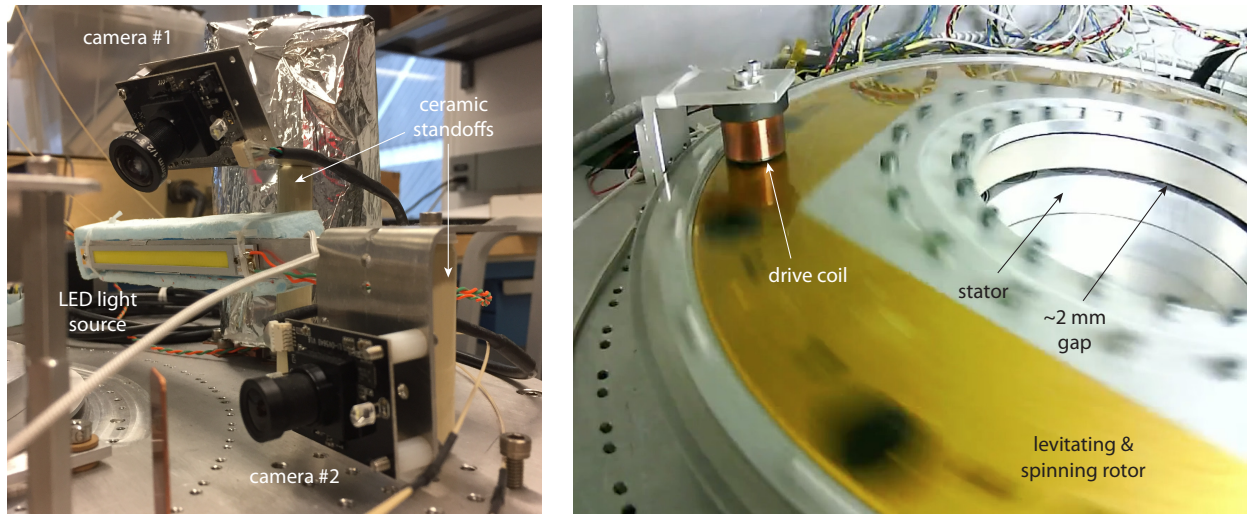


FIG. 5. **Left:** A photograph of the two cameras that are mounted inside the cryostat. These cameras allowed visual monitoring during 50 K operation. **Right:** One frame from a movie that was recorded using camera #1. The rotor is levitating and rotating.

the associated equilibrium temperature falls within the operating range of the camera. The camera modules included white LEDs for subject illumination, but we found them to be too dim. Therefore, we added a 120 mm long white linear LED<sup>43</sup> that has a nominal luminous intensity of 36,600 mcd. The linear LED was not rated for cryogenic operation, so we used a similar thermal circuit to keep it sufficiently warm.

The visibility the cameras provided was particularly useful during the initial stages of the project when the HRM was being developed. As an example, without the cameras it was difficult to know if the rotor released properly when the linear actuator retracted the HRM blades. We discovered early on that the rotor unexpectedly drops approximately 1 mm after release, decreasing the size of the rotor/stator gap. This drop caused a mechanical conflict between early versions of the the rotor and the stator, and this mechanical conflict initially prevented the rotor from turning. The problem was observed through a real-time video stream. Therefore, the cameras helped hone the HRM design by revealing flaws that otherwise would not have been visible.

## B. Speed and Stability

When commissioning the motor, we tested the performance of the PI feedback loop by changing the target rotation frequency in the microcontroller every five minutes and recording the measured rotation frequency as a function of time. Twenty-five minutes of time-ordered data from this test are plotted in Figure 6. The data show that the feedback loop takes approximately 30 seconds to a minute to settle, and then the rotation frequency of the rotor stabilizes to the target rotation frequency. We tested rotation frequencies up to approximately 10 Hz.

When analyzing the data we discovered there is some residual variation in the angular speed after the feedback

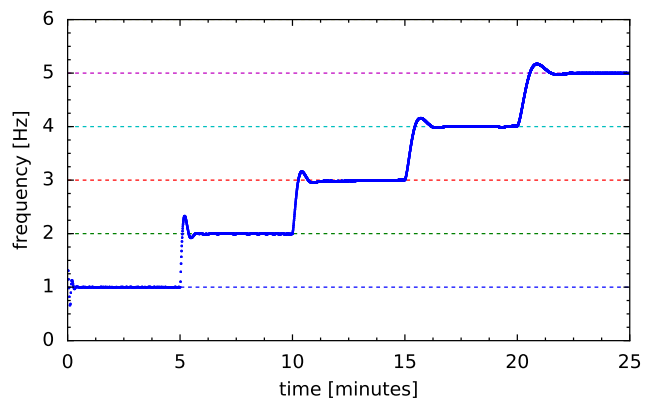


FIG. 6. Rotation frequency as a function of time. The target rotation frequency was changed every 5 minutes. The horizontal dashed lines indicated the target rotation frequencies. After settling, the feedback system successfully maintained the desired rotation frequency. Though the plot shows data for rotation frequencies up to 5 Hz, we tested rotation frequencies up to approximately 10 Hz.

loop has stabilized. This residual variation is approximately

$$\Delta f_0 = \frac{\Delta f_{pp}}{2} \sin(2\pi f_0 t + \phi), \quad (1)$$

where  $\Delta f_{pp}$  is the peak-to-peak speed variation in Hz,  $f_0$  is the rotation frequency in Hz, and  $\phi$  is an arbitrary phase. To clearly show this residual we plotted  $\Delta f_0$  versus orientation angle for several rotational periods in the left panel of Figure 7. For this measurement, the rotation frequency was 7 Hz and  $\Delta f_{pp}$  was approximately 0.06 Hz. Therefore, the rotation speed was stable at the level of  $\pm 0.4\%$ .

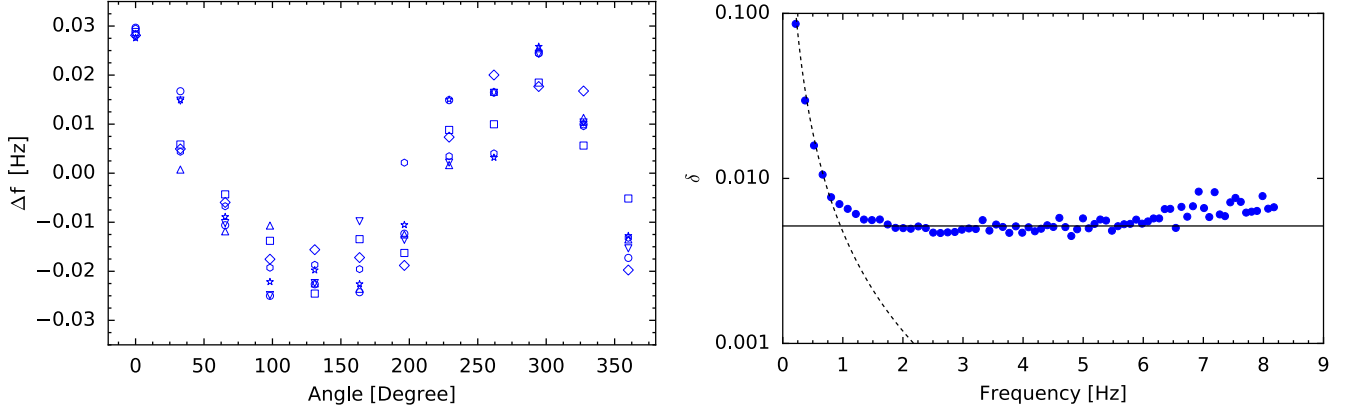


FIG. 7. **Left:** Variation in the rotation frequency as a function of rotor orientation angle for seven periods. For this measurement, the rotor was rotating at 7 Hz (see Section III B). The  $\Delta f_0$  residual, which is approximately sinusoidal, is apparent (see Equation 1). **Right:** Fractional change in the rotation frequency as a function of rotation frequency. The dashed curve is Equation 5 fit to the data below 1 Hz, while the solid curve shows the average value of  $\delta$  between 2 and 6 Hz (see Section III C).

### C. Orientation Uncertainty

Since the encoder disk has 360 slits, it is straightforward to determine the orientation angle of the rotor to within 0.5 deg by simply analyzing the square-wave output from the encoder electronics with a counter. It is possible to decrease this uncertainty by further analyzing the rotation frequency versus time data. Since  $\theta = 2\pi(f_0 + \Delta f_0)t$ , we can integrate to find  $\theta$  as a function of time. Ideally,  $\theta = 2\pi f_0 t$ , but the observed residual angular speed variation term yields an orientation angle deviation  $\Delta\theta$ . If we define the fractional change in rotation frequency as

$$\delta = \frac{\Delta f_{pp}}{f_0} = \frac{f_{max} - f_{min}}{f_0}, \quad (2)$$

then, using Equation 1, the maximum deviation in the angular position of the rotor is

$$\Delta\theta_{max} = \frac{\delta}{2}. \quad (3)$$

The right panel of Figure 7 shows measurements of  $\delta$  as a function of  $f_0$ . There are three distinct regions in the plot: below 2 Hz, above 6 Hz, and in between 2 and 6 Hz. In the region between 2 and 6 Hz, the average value for  $\delta = 5.2 \times 10^{-3}$ , which means  $\Delta\theta_{max} = 0.15$  deg. This orientation angle uncertainty is a conservative estimate, and it meets our performance requirement (see Section I). Above 6 Hz there is a detectable increase in  $\delta$ . This increase is probably due to an observed mechanical resonance near  $\sim 12$  Hz.

Below 2 Hz the data show a  $1/f_0^2$  trend. If we model the interaction between the ring magnet and the magnetic field imprinted in the HTS as a dipole-dipole interaction<sup>14</sup> we can define the fractional speed variation  $\delta$  with respect to the target rotation frequency  $f_0$  as

$$\delta = \frac{\Delta f_{pp}}{f_0} = \sqrt{1 + \frac{\alpha}{f_0^2}} - 1 \quad (4)$$

where  $\alpha$  is a constant related to the physical properties of the system. In the limit  $\alpha/f_0^2 \ll 1$

$$\delta = \frac{\alpha}{2f_0^2}, \quad (5)$$

which has the observed  $1/f_0^2$  dependence. This suggests the low-frequency increase in  $\delta$  is produced by this dipole-dipole interaction. By fitting Equation 5 to the data below 1 Hz we find  $\alpha = 9.5 \times 10^{-3} \text{ Hz}^2$ .

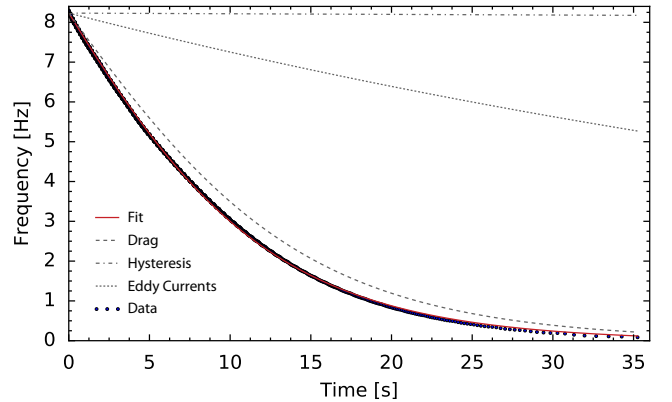


FIG. 8. Spin-down test from 8.5 Hz to 0.2 Hz. Equation 10), which takes into account the three loss mechanisms discussed in Section III D, was fit to the data. The red line is the best-fit model. The gray dashed, dash-dot, and dotted lines represent the three terms of model plotted individually using the best-fit parameters.

### D. Loss

Although the SMB does not have stick-slip friction, other loss mechanisms produce torque that must be overcome by the drive system. To understand the loss mechanisms in the motor, we conducted spin-down tests where we first turned the rotor at 8.5 Hz and then switched off

the drive system. The unwanted torque acting on the rotor caused it to slow down and stop after approximately 35 seconds. Data from one spin-down test is shown in Figure 8. By fitting a theoretical model to this data, it is possible to determine the primary loss mechanism. Our model is composed of three loss mechanisms: hysteresis loss, eddy current loss, and disk-magnet drag.

The drag force due to hysteresis loss<sup>44</sup> scales as

$$F_H \propto \frac{(\Delta B)^3}{J_c}, \quad (6)$$

where  $\Delta B$  is the peak-to-peak change in the magnetic field in the superconductor, and  $J_c$  is the critical current of the superconductor. The drag force due to eddy current loss<sup>45</sup> scales as

$$F_{EC} \propto \sigma(\Delta B)^2 f \quad (7)$$

where  $\sigma$  is the electrical conductivity of surrounding metals and  $f$  is the rotation frequency. For these two loss mechanisms, the changes in the magnetic field come from the intrinsic inhomogeneity in the ring magnet, which ideally is zero. In practice, however, we measured variations in the magnetic field around the ring on the order of a few percent. This inhomogeneity is likely due to manufacturing tolerances. Note that Equation 6 does not depend on the rotation frequency, while Equation 7 has a linear dependence. The proportionality constants are ultimately free parameters in the fit.

The third loss mechanism is produced by the 24 disk magnets used to move the rotor. In general, a magnet moving with constant speed above an infinite conducting plate, will experience magnetic lift and drag forces from the eddy currents induced in the plate. Reitz<sup>46</sup> demonstrates that the drag force is

$$F_D = \frac{3n\mu_0 m^2}{32\pi z_0^4} \frac{w}{v} \left( 1 - \frac{w}{\sqrt{v^2 + w^2}} \right) \quad (8)$$

where  $n$  is the number of magnets,  $v$  is the speed,  $m$  is the magnetic dipole moment,  $z_0$  is the height of the magnet above the plate,  $w = 2/\mu_0 T\sigma$ , and  $T$  is the thickness of the plate. Since the magnets are moving in a circle,  $v = 2\pi f R_{disk}$ , where we assume  $R_{disk}$  is the radial distance between the center of the rotor and the center of each disk magnet (see Figure 2).

When taking into account all three loss mechanisms, the equation of motion for the rotor becomes

$$I \frac{d\omega}{dt} = -R_{disks} F_D - R_{ring} F_H - R_{ring} F_{EC} \quad (9)$$

where  $I = 8.5 \times 10^{-3}$  kg m<sup>2</sup> is the moment of inertia of the rotor, and we assume  $R_{ring}$  is the mean radius of the ring magnet. For our fitting procedure, we are interested in determining  $f$  as a function of time. Therefore, we rearranged Equation 9 to form the more relevant equation of motion:

$$\frac{df}{dt} = A + B f + C F_D(f), \quad (10)$$

where  $F_D(f)$  is simply Equation 8 with  $v = 2\pi f R_{disk}$ , and  $A$ ,  $B$  and  $C$  are the free parameters in the fit. Note

that the unspecified proportionality constants in Equations 6 & 7 are accounted for in the  $A$  and  $B$  fit parameters, respectively.

We used numerical methods to both solve the differential equation and fit the solution to the data in Figure 8. The red line corresponds to the best fit model. Given the values of  $A$ ,  $B$ , and  $C$  from the fit, the gray lines show how the rotor would spin down if only that loss mechanism existed. For example, if we only had hysteresis loss, the rotor would have slowed down an imperceptible amount in 35 seconds. The dominant loss mechanism is disk-magnet drag.

Since the rotational kinetic energy in the rotor is  $I\omega^2/2$ , during spin down, the energy flowing out of the rotor, in watts, is

$$P = \omega I \frac{d\omega}{dt}, \quad (11)$$

which is simply  $\omega$  times Equation 9. During normal operation we keep the rotation frequency constant with the drive system, so the equation of motion becomes

$$I \frac{d\omega}{dt} = 0 = \tau_{drive} - \tau_{loss}, \quad (12)$$

where  $\tau_{drive}$  is the applied torque and  $-\tau_{loss}$  is the right hand side of Equation 9. This indicates that the mechanical power input by the drive system at a given rotation frequency is equal to the power ultimately dissipated into the cryogenic system via  $\tau_{loss}$ . It is desirable to minimize the loading on the cryogenics, so  $\tau_{loss}$  should be minimized. The fit parameters from the spin-down test can be used to calculate  $\tau_{loss}$  for our system, so we can infer the associated heat load on the cryogenics from this measurement.

The top panel of Figure 9 shows the calculated power loss for each individual loss mechanism in  $\tau_{loss}$  as a function of rotation frequency. Power loss from the 24 disk magnets dominates. Looking at the prefactor in Equation 8, this loss can be appreciably reduced by increasing the distance between the disk magnets and the cold plate and decreasing the number of disk magnets on the torque disk. In the bottom panel of Figure 9, we show how the calculation result changes if the number of disk magnets is decreased from 24 to 8, and the distance between the disk magnets and the cold plate is increased from 2 cm to 4 cm. Disk-magnet drag loss decreases by a factor of 48 in this example configuration, and contributes less than the eddy current loss in the SMB itself.

#### IV. DISCUSSION

Our long-term goal is to develop a hollow-shaft, SMB-based motor with a  $\sim 500$  mm aperture that operates at 3 K for next-generation experiments<sup>47,48</sup>. We built and tested the prototype motor presented in this paper to demonstrate the new and more risky subsystems that are needed for the more ambitious large motor. In particular, we were most interested in demonstrating (i) the viability of the scalable HRM design, (ii) the encoder readout approach, and (iii) the idea that the encoder signals can

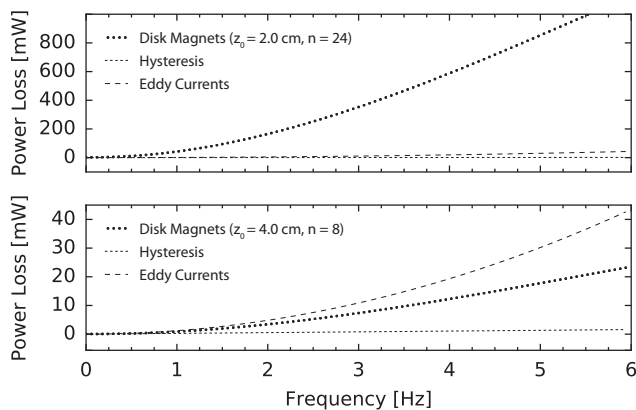


FIG. 9. Calculated power loss as a function of rotation frequency. Points, dotted lines, and dashed lines correspond to contributions from disk-magnet drag loss, hysteresis loss and eddy current loss, respectively. The top panel shows the loss for our configuration ( $z_0 = 2.0$  cm,  $n = 24$ ), and the bottom panel shows the loss for a modified configuration ( $z_0 = 4.0$  cm,  $n = 8$ ) that is designed to reduce the amount of loss from disk-magnet drag.

be used in the feedback loop. The prototype motor test was successful.

Before building the larger motor, several issues need to be addressed. First, the loss from the tested prototype configuration is significant, and it needs to be decreased in future designs. The precise loss requirement will likely depend on the operating temperature choice and whether the future cryogenic system is mechanical-cooler-based or liquid-cryogen-based. Nevertheless, as mentioned in Section III D, the drag-force loss from the disk magnets can be decreased below the eddy current loss in the SMB with straightforward design changes. This target seems reasonable because decreasing the eddy current loss in the SMB will be challenging, so it serves as a fundamental limit. In addition, it may also be worth making the metal structures on the stator out of a superconductor with a transition temperature greater than 3 K, so  $\sigma \rightarrow \infty$ . This change, in principle, makes the disk-magnet drag force zero (see Equation 8). Also, the steel screws that hold the ring magnet in the rotor could introduce a small azimuthal pattern in the magnetic field of the ring magnet ( $\Delta B$  in Equations 6 & 7), which could be a source of the energy loss. This effect should be examined more carefully. Second, one source of heat we did not consider in this study is Joule heating in the coil wire, which can also be appreciable. Making the coils out of superconducting niobium-titanium wire should eliminate this heat source at 3 K. Third, millimeter-wave detector systems can be sensitive to magnetic fields. Therefore, the scaled-up motor should include flux returns and a  $\mu$ -metal enclosure to minimize stray magnetic fields. Fourth, the rotor temperature, or more importantly, the HWP temperature, should be measured during operation. This measurement is difficult because the rotor is levitating. Therefore, a wireless temperature sensor needs to be developed. Fifth, rotor vibration needs to be considered<sup>7</sup>. Finally, the rotor temperature should be as close to the

3 K stator temperature as possible. Some of the light in the telescope beam will be absorbed by the HWP, which introduces a heat load on the levitating rotor. This heat must be removed through radiation, so a radiative heat exchanger between the rotor and the stator needs to be developed.

For the larger motor, it should be possible to decrease the orientation angle uncertainty. For example, if the slit pitch remains constant (2.22 mm) and the encoder disk diameter increases from 254 mm to 508 mm, then there will be a total of 720 slits instead of 360 slits. Therefore, by simply counting slits with the optical fiber encoder sensors, the upper limit on the orientation angle uncertainty decreases from 0.5 deg to 0.25 deg, which is very close to our requirement. This uncertainty can be further decreased, as desired, by increasing the total number of slits, which can be achieved by decreasing the slit pitch further, increasing the encoder disk diameter, or both.

## ACKNOWLEDGMENTS

We would like to thank Robert Rickenbach at Micronor for his assistance and design input regarding the encoder. We would also like to thank Daniel Flanigan, Mark Greenan, David Colavita, and Joshua Sobrin for their help. This project was supported in part by an Italian Space Agency fellowship for Columbro and an NSF Astronomy and Astrophysics Postdoctoral Fellowship for Reichborn-Kjennerud.

- <sup>1</sup>The EBEX Collaboration, A. M. Aboobaker, P. Ade, D. Araujo, F. Aubin, C. Baccigalupi, C. Bao, D. Chapman, J. Didier, M. Dobbs, C. Geach, W. Grainger, S. Hanany, K. Helson, S. Hillbrand, J. Hubmayr, A. Jaffe, B. Johnson, T. Jones, J. Klein, A. Korotkov, A. Lee, L. Levinson, M. Limon, K. MacDermid, T. Matsumura, A. D. Miller, M. Milligan, K. Raach, B. Reichborn-Kjennerud, I. Sagiv, G. Savini, L. Spencer, C. Tucker, G. S. Tucker, B. Westbrook, K. Young, and K. Zilic, *ArXiv e-prints* (2017), arXiv:1703.03847 [astro-ph.IM].
- <sup>2</sup>S. Takakura, M. Aguilar, Y. Akiba, K. Arnold, C. Baccigalupi, D. Barron, S. Beckman, D. Boettger, J. Borrill, S. Chapman, Y. Chinone, A. Cukierman, A. Ducout, T. Elleflot, J. Errard, G. Fabbian, T. Fujino, N. Galitzki, N. Goeckner-Wald, N. W. Halverson, M. Hasegawa, K. Hattori, M. Hazumi, C. Hill, L. Howe, Y. Inoue, A. H. Jaffe, O. Jeong, D. Kaneko, N. Katayama, B. Keating, R. Kesitalo, T. Kisner, N. Krachmalnicoff, A. Kusaka, A. T. Lee, D. Leon, L. Lowry, F. Matsuda, T. Matsumura, M. Navaroli, H. Nishino, H. Paar, J. Peloton, D. Poletti, G. Puglisi, C. L. Reichardt, C. Ross, P. Siritanasak, A. Suzuki, O. Tajima, S. Takatori, and G. Teply, *JCAP* **5**, 008 (2017).
- <sup>3</sup>T. Essinger-Hileman, A. Kusaka, J. W. Appel, S. K. Choi, K. Crowley, S. P. Ho, N. Jarosik, L. A. Page, L. P. Parker, S. Raghunathan, S. M. Simon, S. T. Staggs, and K. Visnjic, *Review of Scientific Instruments* **87**, 094503 (2016).
- <sup>4</sup>S. Bryan, P. Ade, M. Amiri, S. Benton, R. Bihary, J. Bock, J. R. Bond, H. C. Chiang, C. Contaldi, B. Crill, O. Dore, B. Elder, J. Filippini, A. Fraisse, A. Gambrel, N. Gandilo, J. Gudmundsson, M. Hasselfield, M. Halpern, G. Hilton, W. Holmes, V. Hristov, K. Irwin, W. Jones, Z. Kermish, C. Lawrie, C. MacTavish, P. Mason, K. Megerian, L. Monceli, T. Montroy, T. Morford, J. Nagy, C. B. Netterfield, I. Padilla, A. S. Rahlén, C. Reintsema, D. C. Riley, J. Ruhl, M. Runyan, B. Saliwanchik, J. Shariff, J. Soler, A. Trangsrud, C. Tucker, R. Tucker, A. Turner, S. Wen, D. Wiebe, and E. Young, *Review of Scientific Instruments* **87**, 014501 (2016).

- <sup>5</sup>C. A. Hill, S. Beckman, Y. Chinone, N. Goeckner-Wald, M. Hazumi, B. Keating, A. Kusaka, A. T. Lee, F. Matsuda, R. Plambeck, A. Suzuki, and S. Takakura, in *Millimeter, Submillimeter, and Far-Infrared Detectors and Instrumentation for Astronomy VIII*, Proc. SPIE, Vol. 9914 (2016) p. 99142U.
- <sup>6</sup>A. Kusaka, T. Essinger-Hileman, J. W. Appel, P. Gallardo, K. D. Irwin, N. Jarosik, M. R. Nolta, L. A. Page, L. P. Parker, S. Raghunathan, J. L. Sievers, S. M. Simon, S. T. Staggs, and K. Visnjic, *Review of Scientific Instruments* **85**, 024501 (2014).
- <sup>7</sup>B. R. Johnson, J. Collins, M. E. Abroe, P. A. R. Ade, J. Bock, J. Borrill, A. Boscaleri, P. de Bernardis, S. Hanany, A. H. Jaffe, T. Jones, A. T. Lee, L. Levinson, T. Matsumura, B. Rabi, T. Renbarger, P. L. Richards, G. F. Smoot, R. Stompor, H. T. Tran, C. D. Winant, J. H. P. Wu, and J. Zuntz, *ApJ* **665**, 42 (2007).
- <sup>8</sup>B. R. Johnson, *MAXIPOL: A bolometric, balloon-borne experiment for measuring the polarization anisotropy of the cosmic microwave background radiation*, Ph.D. thesis, UNIVERSITY OF MINNESOTA (2004).
- <sup>9</sup>M. L. Brown, A. Challinor, C. E. North, B. R. Johnson, D. O’Dea, and D. Sutton, *MNRAS* **397**, 634 (2009).
- <sup>10</sup>D. O’Dea, A. Challinor, and B. R. Johnson, *MNRAS* **376**, 1767 (2007).
- <sup>11</sup>S. Hanany, T. Matsumura, B. Johnson, T. Jones, J. R. Hull, and K. B. Ma, *IEEE Transactions on Applied Superconductivity* **13**, 2128 (2003).
- <sup>12</sup>T. Matsumura, S. Hanany, J. R. Hull, B. Johnson, and T. Jones, *IEEE Transactions on Applied Superconductivity* **15**, 2316 (2005).
- <sup>13</sup>T. Matsumura, S. Hanany, J. R. Hull, B. Johnson, T. Jones, and P. K. Oxley, *Physica C: Superconductivity* **426431**, Part 1, 746 (2005).
- <sup>14</sup>T. Matsumura, *A cosmic microwave background radiation polarimeter using superconducting magnetic bearings*, Ph.D. thesis, University of Minnesota, Minnesota, USA (2006).
- <sup>15</sup>J. Klein, A. Aboobaker, P. Ade, F. Aubin, C. Baccigalupi, C. Bao, J. Borrill, D. Chapman, J. Didier, M. Dobbs, B. Gold, W. Grainger, S. Hanany, J. Hubmayr, S. Hillbrand, J. Grain, A. Jaffe, B. Johnson, T. Jones, T. Kisner, A. Korotkov, S. Leach, A. Lee, L. Levinson, M. Limon, K. MacDermid, T. Matsumura, A. Miller, M. Milligan, E. Pascale, D. Polsgrove, N. Ponthieu, K. Raach, B. Reichborn-Kjennerud, I. Sagiv, R. Stompor, H. Tran, M. Tristram, G. S. Tucker, A. Yadav, M. Zaldarriaga, and K. Zilic, “A cryogenic half-wave plate polarimeter using a superconducting magnetic bearing,” (2011).
- <sup>16</sup>F. C. Moon, *Superconducting Levitation, Applications to Bearings and Magnetic Transport* (John Wiley & Sons, Inc., 605 Third Avenue, New York, NY 10158-0012, 1994).
- <sup>17</sup>D. C. Araujo, P. A. R. Ade, J. R. Bond, K. J. Bradford, D. Chapman, G. Che, P. K. Day, J. Didier, S. Doyle, H. K. Eriksen, D. Flanigan, C. E. Groppi, S. N. Hillbrand, B. R. Johnson, G. Jones, M. Limon, A. D. Miller, P. Mauskopf, H. McCarrick, T. Mroczkowski, B. Reichborn-Kjennerud, B. Smiley, J. Sobrin, I. K. Wehus, and J. Zmuidzinas, in *Millimeter, Submillimeter, and Far-Infrared Detectors and Instrumentation for Astronomy VII*, Proc. SPIE, Vol. 9153 (2014) p. 91530W.
- <sup>18</sup>B. R. Johnson, P. A. R. Ade, D. Araujo, K. J. Bradford, D. Chapman, P. K. Day, J. Didier, S. Doyle, H. K. Eriksen, D. Flanigan, C. Groppi, S. Hillbrand, G. Jones, M. Limon, P. Mauskopf, H. McCarrick, A. Miller, T. Mroczkowski, B. Reichborn-Kjennerud, B. Smiley, J. Sobrin, I. K. Wehus, and J. Zmuidzinas, *Journal of Low Temperature Physics* **176**, 741 (2014).
- <sup>19</sup>Precision Cryogenics Systems, Model #: PCS 21.0/14.0.
- <sup>20</sup>CTI-Cryogenics, Cryodyne Refrigeration System, Model 350 (two-stage configuration).
- <sup>21</sup>Lake Shore Cryotronics, Inc., Part #: PT-103-AM-2S and Part #: PT-103-AM.
- <sup>22</sup>Lake Shore Cryotronics, Inc., Temperature Monitor, Model 218.
- <sup>23</sup>Pfeiffer D-35164 Asslar turbo pump backed by a BOC Edwards XDS10 dry scroll vacuum pump.
- <sup>24</sup>MDC Vacuum Products, USB K150 DN40 KF FLG MT, Part #: 9173001.
- <sup>25</sup>Douglas Electrical Components, custom fiber optic vacuum feedthrough.
- <sup>26</sup>Ceramtek, 41-pin NW50KF vacuum feedthrough, and Amphe-nol Industrial Operations, 41-pin connector, Part #: PT06SE-20-41S(SR).
- <sup>27</sup>California Fine Wire Company.
- <sup>28</sup>CAN Superconductors, s.r.o., Czech Republic.
- <sup>29</sup>Stycast 2850 FT.
- <sup>30</sup>Applied Magnets, Model #: NR025.
- <sup>31</sup>UltraMotion, Part #: D-A.083-HT17-2-2NO-BR/4-CRYO.
- <sup>32</sup>Applied Motion, Part #: HT17-75.
- <sup>33</sup>Applied Motion, Part #: ST5-Si-NN.
- <sup>34</sup>Micronor Inc.
- <sup>35</sup>Micronor Inc., Fiber Optic Encoder System, Model #: MR320.
- <sup>36</sup>Micronor, Inc., Fiber Optic U-Beam Controller Module, Model #: MR382-1-1.
- <sup>37</sup>TrossenRobotics.com, L298 Dual H-Bridge Motor Driver, Part #: SS-MOT103B1M.
- <sup>38</sup>Moticon, Hollow Core Linear Voice Coil, Part #: HVCM-019-016-003-02-COIL.
- <sup>39</sup>H. McCarrick, D. Flanigan, G. Jones, B. R. Johnson, P. Ade, D. Araujo, K. Bradford, R. Cantor, G. Che, P. Day, S. Doyle, H. Leduc, M. Limon, V. Luu, P. Mauskopf, A. Miller, T. Mroczkowski, C. Tucker, and J. Zmuidzinas, *Review of Scientific Instruments* **85**, 123117 (2014).
- <sup>40</sup>K&J Magnetics, Inc., Part #: D82.
- <sup>41</sup>Leopard Imaging, 5M HD USB Camera, Part #: LI-OV5640-USB-72.
- <sup>42</sup>Isolantite Manufacturing Company, Inc.
- <sup>43</sup>Vollong, 3W White High Power Linear COB LED, Part #: VL-H03W5500380D12.
- <sup>44</sup>C. P. Bean, *Review of Modern Physics* **36**, 31 (1964).
- <sup>45</sup>P. L. Richards and M. Tinkham, *Journal of Applied Physics* **43**, 2680 (1972).
- <sup>46</sup>J. R. Reitz, *Journal of Applied Physics* **41**, 2067 (1970).
- <sup>47</sup>M. H. Abitbol, Z. Ahmed, D. Barron, R. Basu Thakur, A. N. Bender, B. A. Benson, C. A. Bischoff, S. A. Bryan, J. E. Carlstrom, C. L. Chang, D. T. Chuss, A. Cukierman, T. de Haan, M. Dobbs, T. Essinger-Hileman, J. P. Filippini, K. Ganga, J. E. Gudmundsson, N. W. Halverson, S. Hanany, S. W. Henderson, C. A. Hill, S.-P. P. Ho, J. Hubmayr, K. Irwin, O. Jeong, B. R. Johnson, S. A. Kernasovskiy, J. M. Kovac, A. Kusaka, A. T. Lee, S. Maria, P. Mauskopf, J. J. McMahon, L. Monceli, A. W. Nadolski, J. M. Nagy, M. D. Niemack, R. C. O’Brien, S. Padin, S. C. Parshley, C. Pryke, N. A. Roe, K. Rostem, J. Ruhl, S. M. Simon, S. T. Staggs, A. Suzuki, E. R. Switzer, K. L. Thompson, P. Timbie, G. S. Tucker, J. D. Vieira, A. G. Viereg, B. Westbrook, E. J. Wollack, K. W. Yoon, K. S. Young, and E. Y. Young, *ArXiv e-prints* (2017), arXiv:1706.02464 [astro-ph.IM].
- <sup>48</sup>K. N. Abazajian, P. Adshead, Z. Ahmed, S. W. Allen, D. Alonso, K. S. Arnold, C. Baccigalupi, J. G. Bartlett, N. Battaglia, B. A. Benson, C. A. Bischoff, J. Borrill, V. Buza, E. Calabrese, R. Caldwell, J. E. Carlstrom, C. L. Chang, T. M. Crawford, F.-Y. Cyr-Racine, F. De Bernardis, T. de Haan, S. di Serego Alighieri, J. Dunkley, C. Dvorkin, J. Errard, G. Fabbian, S. Feeney, S. Ferraro, J. P. Filippini, R. Flauger, G. M. Fuller, V. Gluscevic, D. Green, D. Grin, E. Grohs, J. W. Henning, J. C. Hill, R. Hlozek, G. Holder, W. Holzappel, W. Hu, K. M. Huffenberger, R. Kesitalo, L. Knox, A. Kosowsky, J. Kovac, E. D. Kovetz, C.-L. Kuo, A. Kusaka, M. Le Jeune, A. T. Lee, M. Lilley, M. Loverde, M. S. Madhavacheril, A. Mantz, D. J. E. Marsh, J. McMahon, P. D. Meerburg, J. Meyers, A. D. Miller, J. B. Munoz, H. N. Nguyen, M. D. Niemack, M. Peloso, J. Peloton, L. Pogosian, C. Pryke, M. Raveri, C. L. Reichardt, G. Rocha, A. Rotti, E. Schaan, M. M. Schmittfull, D. Scott, N. Sehgal, S. Shandera, B. D. Sherwin, T. L. Smith, L. Sorbo, G. D. Starkman, K. T. Story, A. van Engelen, J. D. Vieira, S. Watson, N. Whitehorn, and W. L. Kimmy Wu, *ArXiv e-prints* (2016), arXiv:1610.02743.